This is a repository copy of *Magnetohydrodynamic simulations of spicular jet propagation applied to lower solar atmosphere model. II. Case studies with tilted jets*.

White Rose Research Online URL for this paper:
https://eprints.whiterose.ac.uk/186376/

Version: Published Version

Article:
Dover, F.M., Sharma, R. and Erdélyi, R. (2022) Magnetohydrodynamic simulations of spicular jet propagation applied to lower solar atmosphere model. II. Case studies with tilted jets. The Astrophysical Journal, 929 (1). p. 88. ISSN 0004-637X

https://doi.org/10.3847/1538-4357/ac5aa9

Reuse
This article is distributed under the terms of the Creative Commons Attribution (CC BY) licence. This licence allows you to distribute, remix, tweak, and build upon the work, even commercially, as long as you credit the authors for the original work. More information and the full terms of the licence here:
https://creativecommons.org/licenses/

Takedown
If you consider content in White Rose Research Online to be in breach of UK law, please notify us by emailing eprints@whiterose.ac.uk including the URL of the record and the reason for the withdrawal request.

eprints@whiterose.ac.uk
https://eprints.whiterose.ac.uk/

The Astrophysical Journal, 929:88 (9pp), 2022 April 10 https://doi.org/10.3847/1538-4357/ac5aa9
© 2022. The Author(s). Published by the American Astronomical Society.
OPEN ACCESS

Magnetohydrodynamic Simulations of Spicular Jet Propagation Applied to Lower Solar Atmosphere Model. II. Case Studies with Tilted Jets

Fionnlagh Mackenzie Dover[1], Rahul Sharma[2], and Robertus Erdélyi[1,3,4]
[1] Solar Physics & Space Plasma Research Centre (SP^{2}RC), School of Mathematics and Statistics, The University of Sheffield, Hicks Building, Hounsfield Road, Sheffield, S3 7RH, UK; robertus@sheffield.ac.uk
[2] Department of Mathematics, Physics and Electrical Engineering, Northumbria University, Newcastle Upon Tyne, NE1 8ST, UK
[3] Department of Astronomy, Eötvös Loránd University, Pázmány Péter sétány 1/A, H-1117 Budapest, Hungary
[4] Gyula Bay Zoltán Solar Observatory (GSO), Hungarian Solar Physics Foundation (HSPF), Petőfi tér 3., Gyula, H-5700, Hungary
Received 2022 January 6; revised 2022 February 27; accepted 2022 February 28; published 2022 April 15

Abstract

We report on numerical simulations of a propagating momentum pulse, representing an inclined jet structure in a stratified lower solar atmosphere model. Here, the numerical jets were generated via injection of a momentum pulse misaligned with the radial magnetic field, which resulted in a collimated structure that mimicked the observed inclined jet features in the chromosphere. The influence of inclination angle was examined for a variety of initial driver conditions (amplitude, period) and magnetic field magnitudes to identify their potential role in determining the morphological and dynamical characteristics of chromospheric jets. The numerical jets in our computational domain were consistent with the observed magnitudes of apex height and cross-sectional width for average inclination of chromospheric features. Furthermore, with an increasing misalignment between the momentum pulse and ambient magnetic field, the simulated structures showed a drop in the maximum apex height and length, while an increase in cross-sectional width magnitudes. Our numerical experiments also revealed the development of a *pulse-like* transverse motions in jets along with high density edges/nodes in the direction of jet displacement. It is postulated that dynamic kink instability might be responsible for the observed kinematic behavior of the inclined jet structures in the solar chromosphere.

Unified Astronomy Thesaurus concepts: Solar physics (1476); The Sun (1693); Solar spicules (1525); Solar chromosphere (1479); Magnetohydrodynamical simulations (1966)

Supporting material: animations

1. Introduction

High-resolution observations of solar chromosphere reveal it to be an inhomogeneous layer with structures that outline the magnetic field topology in the region. These structures with both open- and closed-magnetic field topologies emanate from the photosphere and protrude the lower corona through the transition region where plasma beta varies across the unity. Spicules are one of the most common examples of such open-magnetic field topology structures in the chromosphere that appear as slender grass-like features when observed at the limb. These high density ($\sim 10^{10}$–10^{11} cm^{-3}) and relatively cool ($\sim 10^4$ K) gas structures (see review by Tsiropoula et al. 2012) are routinely investigated for their potential role in channelizing mass, energy, and momentum to the lower corona.

It is now established that most of this energy transfer across the transition region via spicules is carried out through magnetohydrodynamic (MHD) waves, with dominant wave modes being reflected in the observed bulk motion of the spicular structures. Imaging-spectroscopy observations suggests three prominent dynamics of spicules viz. transverse, rotational/torsional, and cross-sectional deformations (see Sharma et al. 2018, and references therein). These kinematics are further interpreted as the presence of kink, Alfvén, and sausage wave modes, respectively, in linear MHD approximation (see reviews Zaqarashvili & Erdélyi 2009; Verth & Jess 2016). However, another important aspect of spicule kinematics is associated with mass motions along its structure with velocities ranging between 15 and 110 km s^{-1} for typical lifetimes of around 50–400 s. During this process, the visible apex of observed spicular features attains a maximum height of $\sim$7 Mm and descends back to the surface following a parabolic trajectory (Pereira et al. 2012, 2016).

These plasma flows in spicules not only contribute to the average mass flux of the corona and the solar wind, but also play an important role in the stability of the structure itself. Mass motions deviated from the ambient magnetic field and/or at local curvature of the spicule structure can induce transverse displacement of the feature akin to the MHD kink wave mode (Zaqarashvili 2020; 2021). Meanwhile, field-aligned plasma flows can generate cross-sectional width deformations resembling sausage wave modes and further modulate the periodicity of the observed width variations (Mackenzie Dover et al. 2020, 2021). However, it must be noted that these flows are guided by the magnetic fields in the chromospheric environment which are highly complex with varied degrees of inclination to the normal. This condition leads to misalignment between the observed mass flows and the magnetic field pertinent to the structure and/or the background.

Previous studies provided a crude estimate of the magnitude of the misalignment between an observed chromospheric structure and its ambient magnetic fields using multi-wavelength spectropolarimetric inversions. de la Cruz Rodríguez & Socas-Navarro (2011) used Ca II observations of chromospheric fibrils and found a significant number of cases with strong misalignment (>45°). However, subsequent

Original content from this work may be used under the terms of the Creative Commons Attribution 4.0 licence. Any further distribution of this work must maintain attribution to the author(s) and the title of the work, journal citation and DOI.

investigations (Schad et al. 2013; Asensio Ramos et al. 2017), though, also found indications of misalignment between the observed features and estimated magnetic field vectors, but with lower deviation in the range 10°–34°. Here, it must be noted that the difference in estimated misalignment angles could be attributed to the noisy Stokes polarization for chromospheric data sets and/or inversion techniques. Petralia et al. (2018) examined misalignment between mass flows and magnetic structures and highlighted its potential role in the observed fragmentation of plasma substructures.

The deviation between chromospheric magnetic field and structures were also investigated using advanced MHD numerical simulations involving radiative transfer mechanisms. Leenaarts et al. (2015) used 3D numerical simulations to compare the chromospheric magnetic field topology with fibril structures in Hα passband and reported misalignment between the vertical component of the magnetic field and the fibril structures. Furthermore, Martínez-Sykora et al. (2016) used 2.5D radiative MHD simulations that included ion-neutral interaction effects. The authors suggested prominent misalignment at sites of strong ambipolar diffusion, resulting due to decoupling between ions and neutrals in the chromospheric environment.

This paper is a step forward from our earlier work (Mackenzie Dover et al. 2020, 2021), where the response of field-aligned plasma flow on the observed dynamics of simulated jet structure in a stratified lower solar atmosphere were investigated. Here, we aim to examine the role of *misalignment/tilt between the background magnetic field and momentum pulse* to identify the modifications in the observed kinematics of the simulated jets akin to type I spicules. An improved jet-tracking algorithm is used to trace the dynamics of the jet structure, along with quantification of parameter magnitudes to assess their influence over the morphological and kinematic behavior of the simulated spicule feature.

2. Method

The computational model used in the numerical simulations employed a grid-adaptive MPI-AMRVAC version 2.0 software (Tóth 1996; Keppens et al. 2012; Porth et al. 2014; Xia et al. 2018) in 2D settings. The governing MHD equations and the equilibrium atmosphere for the simulated type I spicule structure remains the same as described in detail in Section 2, of Mackenzie Dover et al. (2021). However, two main changes had been made in the driver and the jet-tracking algorithm. Here, the flow was injected at the base of the computational domain at an angle to the normal with modified driver profile given as

$$\begin{pmatrix} v_x \\ v_y \end{pmatrix} = \frac{-A}{2}\begin{pmatrix} \sin\theta \\ \cos\theta \end{pmatrix}\left(\tanh\left(\frac{\pi(t-P)}{P}+\pi\right)+1\right) \times \exp\left(-\left(\frac{x-x_0}{\Delta x}\right)^2\right), \quad (1)$$

where v_x and v_y are the horizontal and vertical velocity, respectively, A is the amplitude of the driver, P is the driver time, t is time, x is horizontal position, x_0 is the location of the central jet axis, θ is the launch/misalignment angle, while the Δx is based on the FWHM of the cross-sectional width of the simulated jet and is given by

$$\Delta x = \frac{j_w}{2\sqrt{2\log 2}}, \quad (2)$$

where $j_w = 187.5$ km is the jet width.

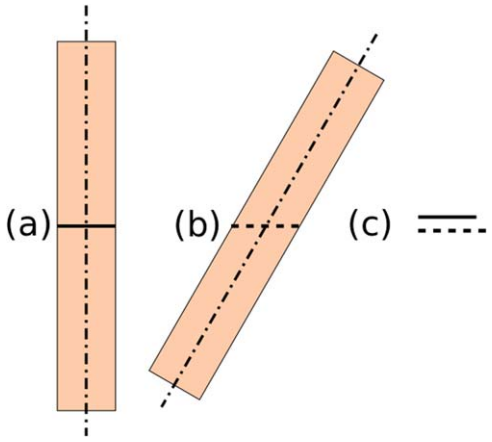

Figure 1. Cartoon depicting the variations in cross-sectional width estimates for inclined structures. The rectangles provide a crude depiction of chromospheric jets with respective axis marked by a dashed–dotted line. The cross section of these features, vertical (a) and inclined (b), are shown via solid and dashed lines, respectively. The changes in these estimates due to inclination are compared in (c).

Modifications had also been made to the jet-tracking algorithm which was used to capture the morphological evolution (maximum height, length, cross-sectional width) of the simulated structure for accurate estimation of these parameters due to prescribed inclination in the jet dynamics. It must be noted that earlier studies (Mackenzie Dover et al. 2020, 2021) analyzed the estimated morphological parameters of the jet structures simulated without any inclination with respect to the background magnetic field. In other words, the central axis of the jet structure remained aligned with the normal to the photospheric layer situated at the bottom of the computational domain. There, any time–distance slit across the jet would remained perpendicular to the central axis of the structure (see Figure 1(a)) and provided an estimate of cross-sectional width at that height. However, for an oblique structure (Figure 1(b)), or at regions in jet with local curvature, the central axis of the jet no longer remained perpendicular to the normal and an application of similar time–distance slit might gave erroneous estimation, therefore artificially altering the width estimates (Figure 1(c)).

To overcome this problem, the improved algorithm tracked the variations in the central axis (yellow stars) of the simulated jet structure (Figure 2) over length. First, a tracer was used to track the fluid advection (akin to using a dye to track fluid flow), which was then converted into a binary image using the method outlined in Mackenzie Dover et al. (2021). For correct slit placement, perpendicular to the jet, the central axis was tracked by finding the midpoint of multiple horizontal slits taken every 0.1 Mm of the jet length as shown by the yellow stars on Figure 2. Further, to keep the artificial slits at a consistent position over time, they vary in height, but remain fixed in terms of jet length, where a slit is placed at every 1 Mm of length. Next, the angle of the jet tilt from the vertical was estimated at every slit location by calculating the angle between the closest location of the jet central axis at each megameter of jet length and its upper neighbor. It must be noted that each slit

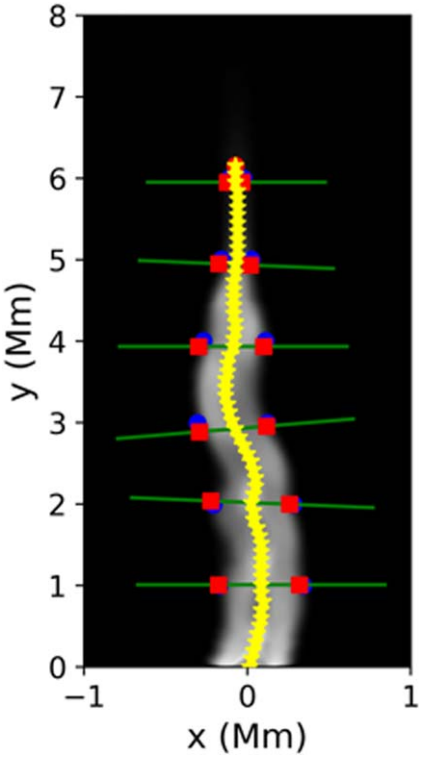

Figure 2. Image showing an example of improved jet-tracking software developed for the accurate estimation of morphological characteristics of a jet structure with an inclination of $\theta = 10°$. The central axis is highlighted by yellow stars over its length while the edges of the simulated jet marked by blue dots. Time–distance slit (green) across the structure estimates the relative tilt at the given height to account for the modified edge. The corrected edge are highlighted by red squares. A 22 s animation shows the dynamics tracking of the jet.

(An animation of this figure is available.)

was placed perpendicular to its local tilt angle relative the jet's central axis. Here, to achieve width measurement, the values along the slit were interpolated from the grid and then a gradient was taken to identify the edges. In case, if only one edge was found, the search box was widened approximately $60 \times 50\,\mathrm{km}^2$ and the process was repeated until both the edges were located. The solid blue dots in Figure 2 highlight the method of horizontal slits at every 1 Mm of height as carried out in Mackenzie Dover et al. (2020, 2021). Throughout the present work, the analysis from both methods were discussed and are referred to as *traced* slits when correcting for tilt angles, while, *horizontal* slits when using the earlier methods described in Mackenzie Dover et al. (2020, 2021).

3. Results and Discussion

3.1. Parameter Benchmarking

The choice of initial parameter magnitudes to simulate the type I spicule were taken from Mackenzie Dover et al. (2021). Distinct combinations of these selected parameters were then subdivided into two groups (P1 and P2), with each set having a driver period of 300 s, comparable to the lifetime of a spicule in the quiet-Sun chromosphere. The prime objective of these subgroups was to benchmark the influence of different parameter magnitudes over the observed morphological characteristics (height, width) and also to compare the results with a *standard jet* (Mackenzie Dover et al. 2021) in an idealized stratified lower solar atmosphere. First subgroup (P1) tested the relation between the simulation parameters for varying degrees of inclination ($\theta = 0°$, 5°, 15°), mimicking the multitude of magnetic field tilt in the solar chromosphere. Moreover, the cross-sectional width estimates derived from improved tracking algorithm were also compared with earlier method (Mackenzie Dover et al. 2021), to provide a much accurate measure of jet deformations in structure with misaligned magnetic field and plasma motions. Whereas the second group (P2) remained purely focused on the effect of the misalignment ($\theta = 0°$–60°) for a standard jet condition ($P = 300$ s, $A = 60$ km s^{-1}, $B = 60$ G) in the lower solar atmosphere. Furthermore, this benchmark intended to gain a better insight into the longitudinal dynamics of the misaligned plasma motions and a comparison to the observed jet features in the chromosphere. A summary of the parameters used in the simulations are given in Table 1.

Table 1
Two Sets (P1 and P2) of Parameter Magnitudes, Including Driver Lifetimes (P), Velocity Amplitude (A), Magnetic Field Strength (B), and Corresponding Inclination Angles for Simulated Jet Structure

Parameter Scan	P (s)	A (km s^{-1})	B (G)	θ (°)
P1	300	20, 40, 60	20, 40, 60, 80	0, 5, 15
P2	300	60	60	0, 5, 10, ..., 60

3.1.1. Parameter Set: P1

Figure 3 show the results of simulations using parameter set P1, which employed a horizontal slit over the jet structure. Here, for varying degrees of misalignment (θ) between the magnetic field and an injected momentum pulse, the morphological characteristics (maximum height, mean width) of the simulated jet were examined. The influence of two key parameters, magnetic field strength (B) and driver amplitude (A), were investigated to assess their role in governing the observed physical behavior of the jet structure. In these simulations, a uniform vertical magnetic field was applied and the range of values of B is consistent with observed magnetic field strengths (Centeno et al. 2010; Suárez et al. 2015; Kriginsky et al. 2020). At $\theta = 0°$, where the momentum pulse was aligned with the radial magnetic field, the general trends for both parameters (B, A) were in agreement with the results from Mackenzie Dover et al. (2021). However, with the addition of a tilt in the background magnetic field, which further created a misalignment with the injected mass flows, there were noticeable effects on the maximum heights and the mean cross-sectional widths of the jet structure.

Figure 3(a) highlights the variations in maximum height and the magnetic field magnitude (B) for different sets of driver amplitude ($A = 20$, 40, 60 km s^{-1}) and misalignment angles ($\theta = 0°$, 5°, 15°). Here, for a small driver amplitude (20 km s^{-1}), the maximum height of the structure remained negligible, irrespective of the tilt and magnetic field magnitudes; however, for $A = 40$ km s^{-1}, the jet rose to a maximum height below 4 Mm with a small change at $B = 40$ G. Interestingly, for a large driver amplitude (60 km s^{-1}), the jet attained a height in the range of 6–8 Mm, but was complemented by a significant drop for misalignment angle ($\theta = 15°$) and magnetic field strength ($B = 60$ G). For mean cross-sectional widths (Figure 3(b)), with an increase in the magnitude of the magnetic field strength (B), the jet structure

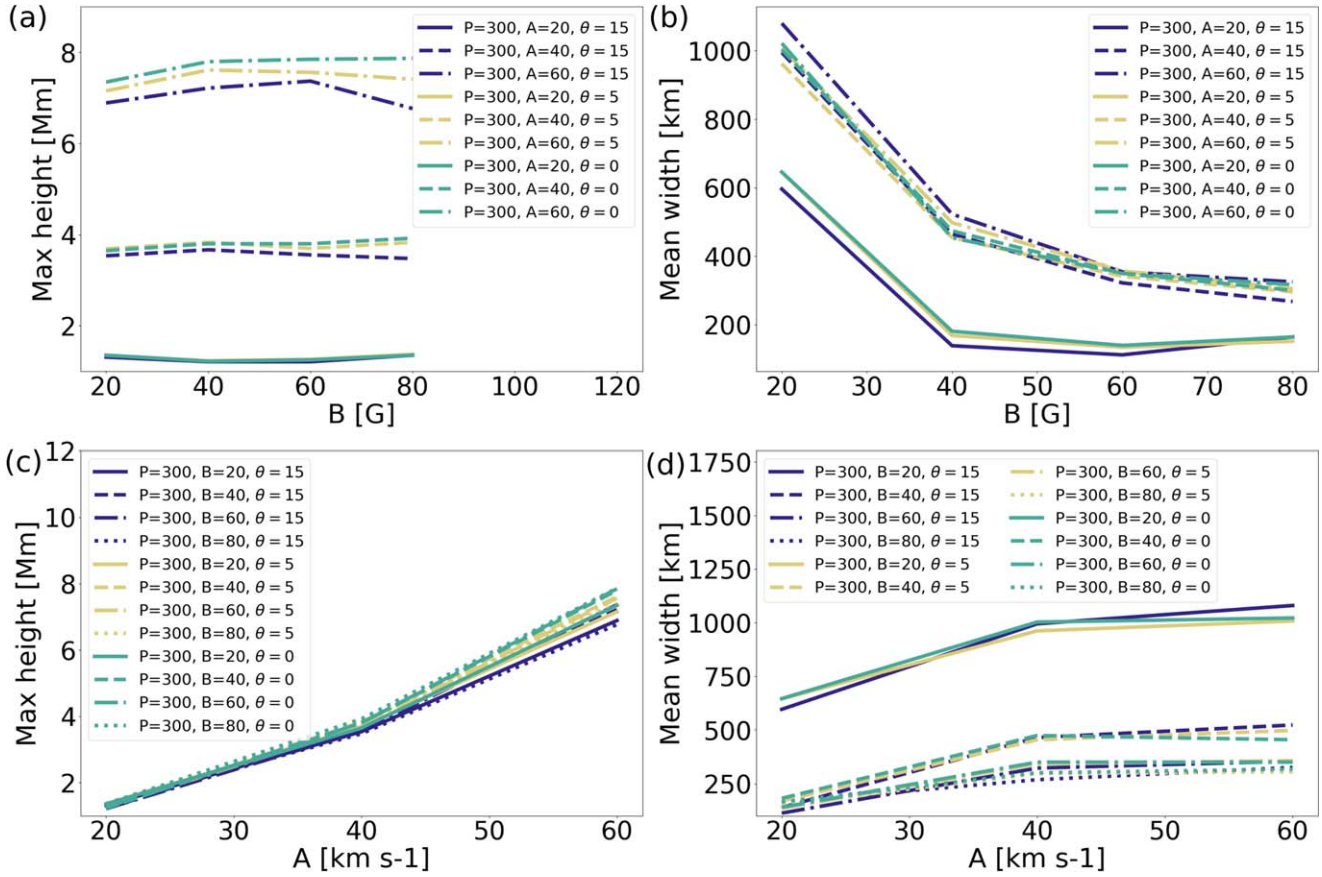

Figure 3. Panels comparing the effects of a combination of misalignment angles (θ) and simulation parameters (top–bottom: magnetic field strength, driver amplitude) on the maximum apex height (left) and mean cross-sectional widths (right) for the jet structure. Here, it must be noted that the cross-sectional widths are estimated using a horizontal (uncorrected) slit, across the density of the simulated structure.

showed a common trend with a continuous decrease in width, along with prominent changes at 40 and 60 G.

Figures 3(c) and (d) display variations in maximum height and mean cross-sectional widths and driver amplitude (A). The maximum height of the simulated jet structure showed an increasing trend with rise in the magnitude of the momentum pulse. This behavior was consistent for all degrees of misalignment angles between the injected flow and the magnetic field, however, with an apparent divergence at $A > 40$ km s^{-1} (Figure 3(c)). A similar trend was noted for the mean cross-sectional width parameter (Figure 3(d)), which showed a sharp increase in its magnitude until $A = 40$ km s^{-1}, followed by a near constant value with rise in the driver amplitude. Here, it should also be noted that the jet appeared comparatively slender (<500 km) for magnetic field strength, $B > 20$ G for all variations in the misalignment angle (θ) and the driver amplitude (A).

The analysis was repeated using the improved algorithm to accurately estimate the cross-sectional width of the inclined jet structure. Moreover, instead of the apex height of the jet, the maximum length of the feature was examined for aforementioned combination of simulation parameters. Figure 4(a) shows a similar trend for jet length for a combination of magnetic field strength (B), driver amplitude (A), and misalignment angles (θ), though with an exception to parameter set $P = 300$ s, $A = 60$ km s^{-1}, and $\theta = 15°$ when compared to apex height. Estimated cross-sectional widths (Figure 4(b)) using traced slits displayed identical behavior with horizontal slits (Figure 3(b)), however, with a slight improvement in width magnitudes. The variations in maximum length, mean widths, and driver amplitudes (Figures 4(c), (d)) also highlighted profound changes in parameter behavior at $A = 40$ km s^{-1}. The mean cross-sectional widths for highly inclined jets ($\theta = 15°$) with magnetic field strength, $B = 20$ G, showed a sharp decrease in their magnitude for driver amplitudes >40 km s^{-1}.

3.1.2. Parameter Set: P2

The effect of misalignment angles over the morphological and kinematic parameters of a *standard jet* are quantified here. The jet had varying inclination angles ($\theta = 0°$–$60°$) with a constant driver amplitude ($A = 60$ km s^{-1}), period ($P = 300$ s), and magnetic field strength ($B = 60$ G) magnitude for all numerical tests.

Figure 5(a) shows the influence of increasing misalignment angles over maximum height, length, and cross-sectional width estimates. Simulations suggest a steep decrease in height and length magnitudes that became noticeable at $\theta = 20°$. Here, it must be noted that most of the observed type I spicule structures show an inclination with the normal inclination in the range of 20°–30° (Tsiropoula et al. 2012), whereas the decrease in height and length magnitudes were prominent following this range in our simulations. Also, there was a noticeable difference between the magnitudes of maximum height and length with increasing misalignment angles, implying presence of slightly longer jet structures at lower heights. Furthermore, these results also support the fact that longer/higher jets tend to

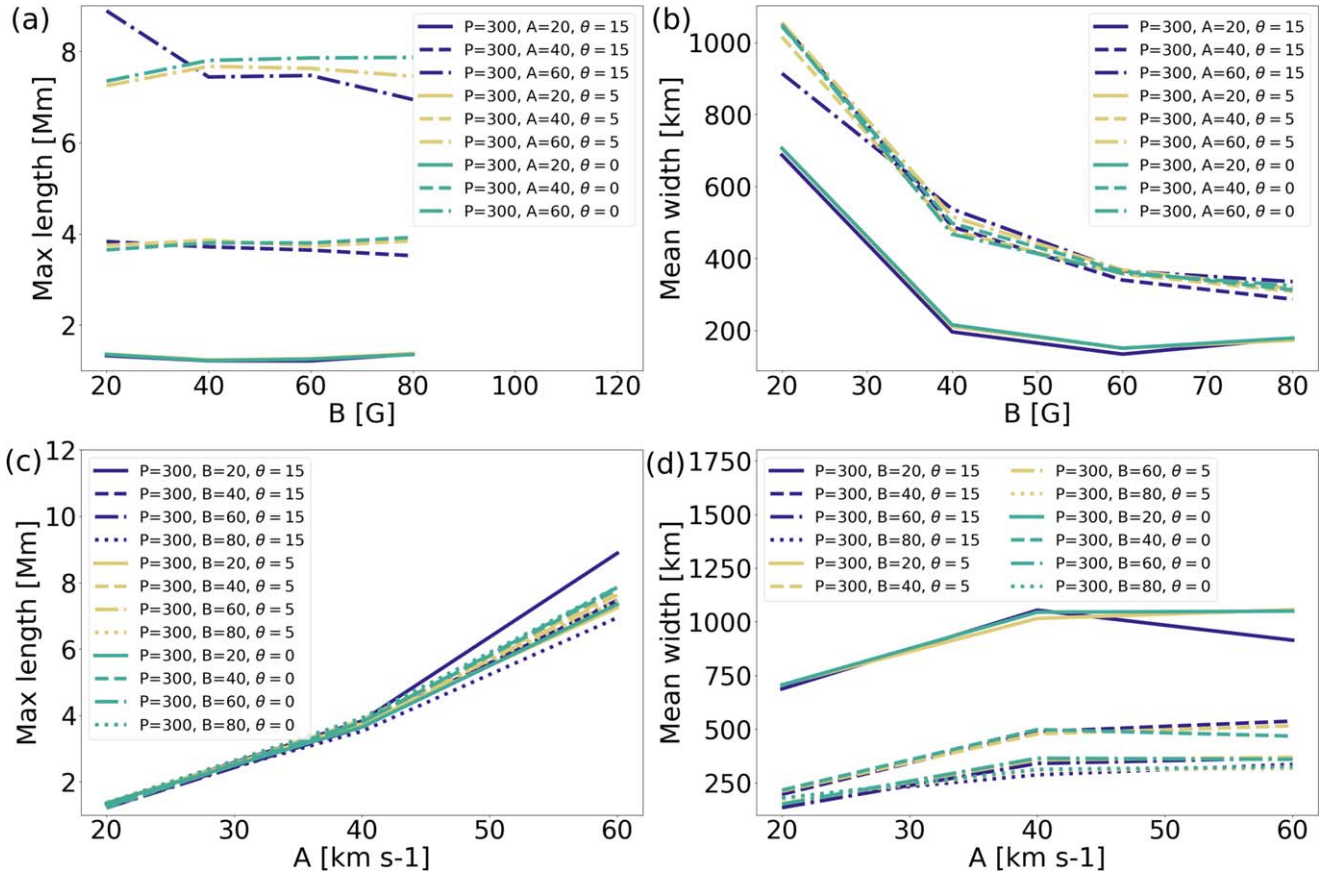

Figure 4. Similar to Figure 3, however, the cross-sectional widths are estimated using a traced (corrected) slit over the density structure of the simulated jet.

appear in coronal holes (low θ) as compared to quiet-Sun (moderate θ) and active region (high θ) jets.

The estimated cross-sectional widths using both horizontal (uncorrected) and traced (corrected) slits over the density structure of the simulated jet(s) showed an increasing trend with the rise in misalignment angles (Figure 5(a)). These increases in width estimates were distinct in the range of $\theta = 20°$–$45°$, followed by an intermittent drop in magnitude. Both methods (horizontal and traced) displayed a common trend in width parameter; however, the traced slit consistently estimated higher magnitudes of jet width. At $\theta = 20°$, the mean cross-sectional width estimates from both methods were in the range of 350–400 km, which is consistent with the reported magnitudes (∼360 km) of observed widths for on-disk fibril structures (Morton et al. 2012). For higher misalignment angles (e.g., $\theta = 50°$, $60°$), there was a drop in width estimates along with height and length parameters. These results indicate the ubiquity of highly inclined, slender jet features at lower heights in the solar atmosphere.

A noteworthy implication of these results is associated with the appearance of spicular jet structures at different heights/lengths for a variety of misalignment/inclination angles. Observations indicate multitude of chromospheric jet species (mottles, spicules, fibrils, etc.) with different morphological characteristics (see review in Tsiropoula et al. 2012), which are believed to be generated by distinct physical mechanisms (Sterling 2000). Our results hint toward the possibility that observed chromospheric jets might have a common generation mechanism with observed morphological differences arising due to their location and inclination with respect to the ambient magnetic field topology.

3.2. Jet Dynamics

Observational studies (Sharma et al. 2018, and references therein) indicated that chromospheric jets display complex/coupled dynamical characteristics that include periodic transverse, cross-sectional width deformations and rotational motions. Evolution of density estimates of simulated structures were examined to identify the dominant bulk motions in jets, while quantifying the role of misalignment between magnetic field and initial momentum pulse in subsequent evolution of bulk dynamics over time and space.

3.2.1. Longitudinal Motions

Figures 5(b) and (c) highlight the temporal evolution of longitudinal motions of the jet's apex height and length parameters for varying misalignment angles. Simulated jet structure showed a clear parabolic trajectory with a decrease in its apex height/length over increasing misalignment angles (θ). Parabolic motions are a common component observed in spicules (De Pontieu et al. 2007; Martínez-Sykora et al. 2009; Anan et al. 2010; Pereira et al. 2014; Skogsrud et al. 2015). The maximum length of the jet attained a higher magnitude as compared to the apex height for misalignment angles >20°. For any $\theta > 50°$, the longitudinal motions of the jet, along its height and length, deviated from an ideal parabolic path and showed a tailed attenuation at height/length < 3 Mm.

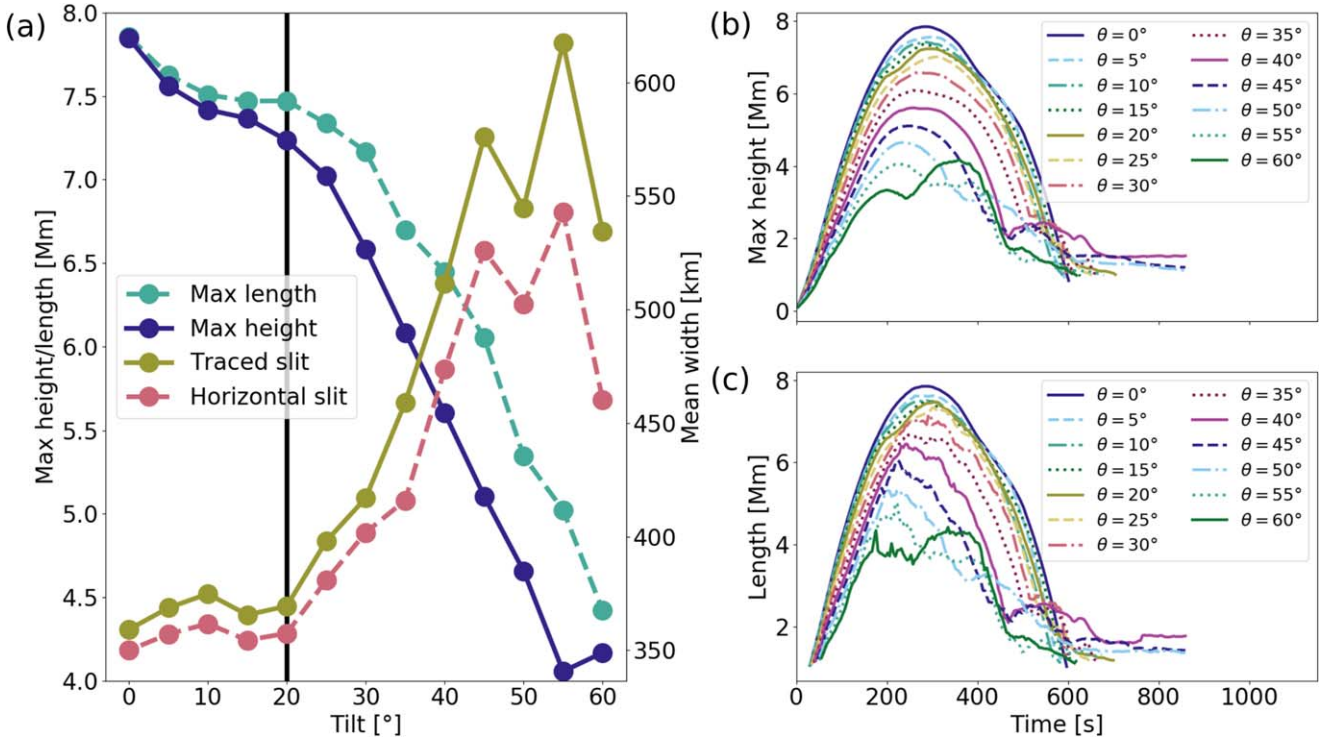

Figure 5. Influence of misalignment angles over the morphological and dynamical characteristics of simulated type I spicule structures. Panel (a) shows the variations in jets height, length, and mean cross-sectional width with increasing tilt angle (θ). The average inclination angle ($\theta = 20°$) for the observed limb spicules (Beckers 1968) is highlighted by a vertical black line. Panels (b) and (c) showcase the effects of misalignment angles for parabolic longitudinal motions of the jets over time for its maximum height (b) and length (c) parameters.

3.2.2. Transverse Motions

Figures 6 and 7 showcase the density evolution of the simulated jet structure for various misalignment angles in the range of 0°–25° to the normal alignment. Our simulation results highlight distinct kinematic and morphological characteristics of the jet, which are augmented with an increasing misalignment angle between the background magnetic field and the simulated feature. Figures 6(a)–(d) show the jet formed due to a momentum pulse launched aligned ($\theta = 0°$) with the magnetic field. This *standard jet* showed typical internal substructures with crisscross/knot-like patterns, together with a bright apex as discussed in detail by Mackenzie Dover et al. (2021). However, with the inception of a small tilt ($\theta = 5°$), the jet morphology showed subtle changes (Figures 6(e)–(h)), particularly during the fall phase of the plasma. Initially in the rise phase, the jet axis showed small amplitude kink motions (Figure 6(f), $t = 223$ s) propagating through the jet structure. These motions ascend along the axis and retarded prior to the driver switch-off at $t = 300$ s, resulting in a significant plasma coagulation and/or mixing within the jet beam (Figure 6(g), $t = 288$ s), below the bright bulb-like apex. Similar behavior with slightly higher kink motion was also evident for the jet inclined at $\theta = 10°$ (Figures 6(i)–(l)), with plasma descending along with the jet structure ($t = 425$ s) toward the end of the jet lifetime.

The kink motions at the jet axis further amplified with the increase in the misalignment angles of the structures. At this stage, these kink motions no longer remained confined to the jet axis but resulted in the transverse displacement of the jet body perpendicular to the plasma flow. Figures 7(a)–(d) highlight the dynamics of the jet feature tilted at an angle of $\theta = 15°$, where the jet body is displaced perpendicular to the axis (Figures 7(b), (c)). The leading edge/nodes of the jet showed higher plasma densities as compared to the trailing edge, along with density depletion (cavity) near the central axis of the jet. The trailing edge of the feature showed signatures of instabilities similar to previously reported Kelvin–Helmholtz instability for chromospheric jet structures (Kuridze et al. 2016; Antolin et al. 2018). These distinct characteristics were common for all simulated structures with higher ($\theta \geqslant 20°$) misalignment angles (Figures 7(e)–(l)).

The rise in displacement amplitudes with increase in the misalignment angles between the jet and radial magnetic field was also evident from time–distance (TD) analysis of jet motions.

Figure 8 shows TD cross cuts for inclined jets ($\theta = 0°$–$55°$) with an artificial slit placed at a height of 1 Mm from the base of each of the simulation. For the *standard jet* ($\theta = 0°$), there was no transverse displacement in the structure, though, a clear indication of a cavity within the jet beam evolving over time. However, with some misalignment ($\theta = 5°$), there were signatures of transverse displacements, which continued to grow with tilt angles. These single *pulse-like* displacements in spicules, akin to the ideal MHD kink wave mode ($m = 0$), were also reported by Sharma et al. (2018), though the physical mechanism responsible for such behavior remained unclear due to observational constraints. Moreover, for higher misalignment angles ($\theta > 25°$), the leading edges/nodes had a higher density resulting from the plasma pileup due to perturbed magnetic field, channelizing the flow of plasma to maintain local equilibrium. Furthermore, over time, there was a strong depletion in plasma densities for jets inclined at angles, $\theta > 45°$, suggesting low plasma upflow in highly inclined chromospheric jets.

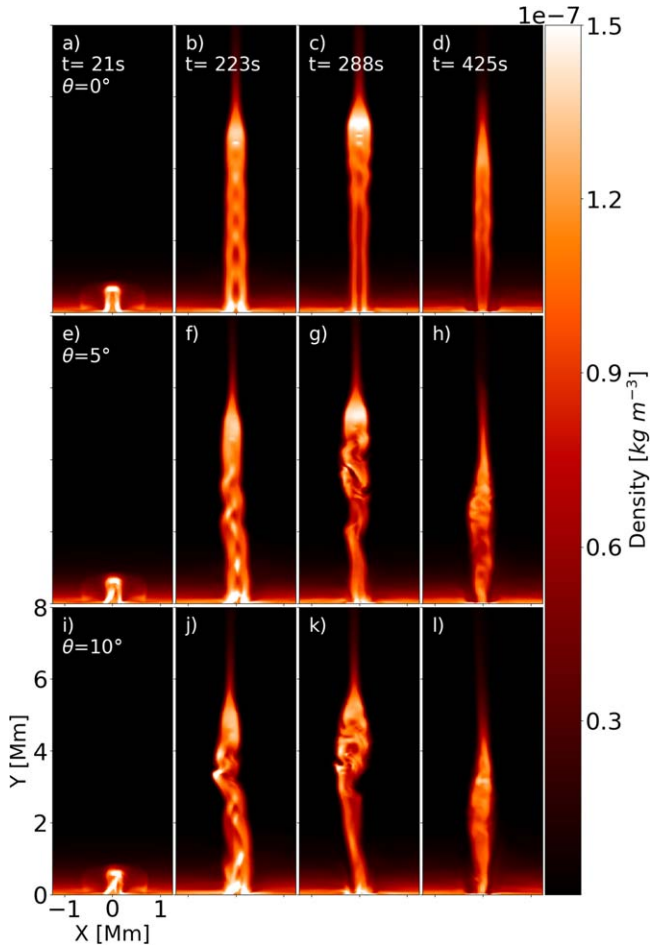

Figure 6. Temporal evolution of density structure of the simulated type I spicule jets for different misalignment angles. Top panels (a)–(d) show the *standard* jet feature at time (t) = 21, 223, 288, and 425 s, with distinct internal substructures and a bright apex. Middle panels (e)–(h) show the jet at same time steps with misalignment angle (θ) = 5°, with a noticeable kink motion of the jet axis. Bottom panels (i)–(l) show similar behavior for a higher misalignment angle (θ = 10°). The animation runs from t = 0–601.1 s.

(An animation of this figure is available.)

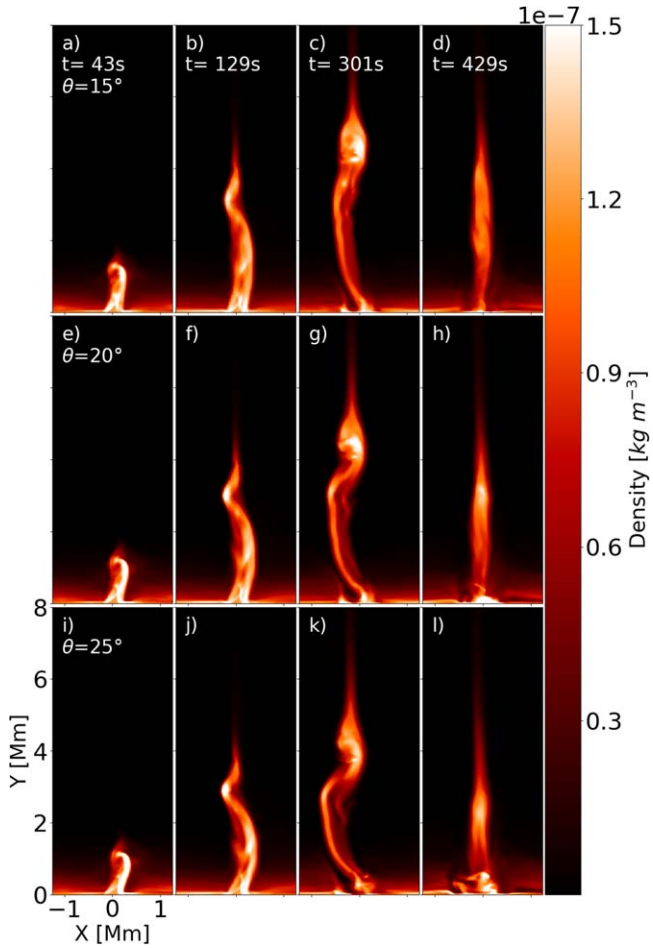

Figure 7. Similar to Figure 6, the panels show the evolution of the density structure of the jet for misalignment angles (θ) = 15°, 20°, and 25° at time steps 43, 129, 301, and 429 s. Top panels (a)–(d) highlight the jet dynamics for plasma flow misaligned at an angle θ = 15°, with respect to the background magnetic field. The central axis of the jet is displaced from its mean position, akin to swaying motion of observed spicule features. Similar behavior with comparatively high displacement is noticeable for simulated jet structures, misaligned at θ = 20° (middle panels (e)–(h)) and θ = 25° (bottom panels (i)–(l)), respectively. The animation runs from t = 0–601.1 s.

(An animation of this figure is available.)

One possible mechanism to explain these *pulse-like* transverse motions in misaligned jets is the dynamic kink instability (DKI; Zaqarashvili 2020) proposed for chromospheric spicules. Triggering of this instability is attributed to the dominance of centripetal forces over the Lorentz force in regions where spicular structures are deviated from the vertical magnetic fields. The centripetal forces tend to push the plasma radially outward from the jet axis while the Lorentz force tries to compensate for the same to maintain the local equilibrium. At regions where the jet structure is inclined and/or has a local curvature, the centripetal force deforms the jet boundary while amplifying the transverse component of the plasma motions. Here, the flow along the jet becomes super-Alfvénic and can lead to the rise of DKI, which is reflected as enhancement in transverse displacements. Zaqarashvili (2020) further postulated that more inclined jets will showcase higher transverse motions, which is consistent with our simulations (Figure 8).

Furthermore, an interesting aspect of these TD plots is the appearance of thread-like density strands for transverse motions over time. These strands were more prominent during initial phase of the evolution (Figure 8, ∼0–200 s) of jets, misaligned for $\theta \geqslant 10°$. Similar strands in TD plots of chromospheric jets were reported by, e.g., Liu et al. (2009 and Chen et al. (2012), where the authors interpreted these observations as unwinding helical threads, as proposed by Shibata & Uchida (1985, 1986) and Canfield et al. (1996). Here, our simulations provide an alternate explanation of this behavior where magnetic field itself regulates the plasma motions, without any prior necessity for the release/transportation of stored twists and/or helicity.

3.3. Cross-sectional Width Modulations and Effects of Spatial Resolution

Previous studies by Mackenzie Dover et al. (2020, 2021) examined the variations in cross-sectional width estimates in numerical jets and highlighted the role of field-aligned plasma motions in modulating the kinematic and morphological characteristics of spicules. The authors concluded that (field-aligned) flows can influence the periodicity associated with width estimates during both ascending (rise) and descending (fall) phases, but can also result in crisscross patterns within the jet structure along with a bright bulb-like apex due to superimposition on shock waves. Figures 6(a)–(d) show these

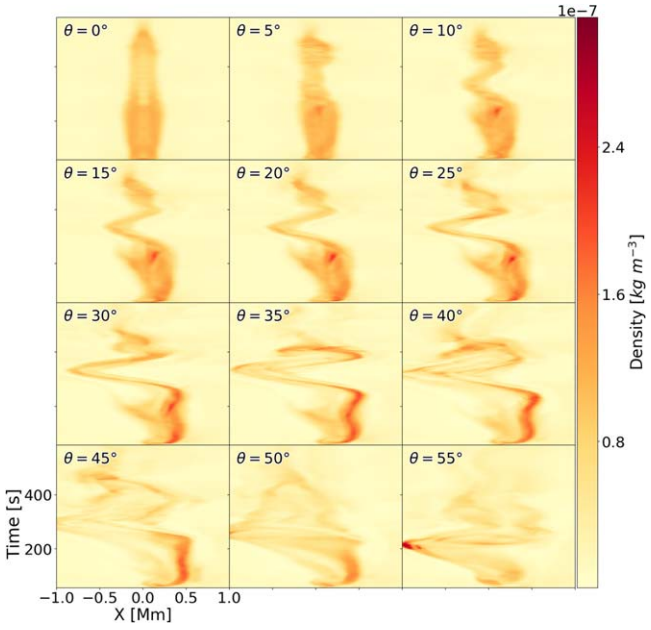

Figure 8. Panels show the TD evolution of the density structure for the misaligned jet feature using an artificial slit, placed at a height of 1 Mm from the base of the computational domain. The displacement of the jet axis is clearly evident for misalignment angles over 10°, along with concurrent cross-sectional width deformations. Also, indications of strong depletion in the density structure of the jet for angles >45°.

substructures at the site of width deformations in the non-inclined jet along with a bright apex.

However, with a small misalignment ($\theta = 5°$) between the momentum pulse and the ambient magnetic field, crisscross patterns tend to deliquesce at the jet axis for kink motions that further grew with the rise in misalignment angle. The simulated jet still developed plasma coagulation at the site(s) of crisscross patterns (Figures 6(f), (j)) during the rise phase for relatively smaller misalignment angles ($\theta = 5°$, 10°). Moreover, for higher tilt angles ($\theta = 15°$–$25°$), these plasma concentrations tend to move along the jet axis to form bright edges/nodes in the direction of jet displacement. Despite a varying degree of misalignment angles, the simulated jet structures maintained a bright bulb-like apex (Figures 6, 7(c), (g), (k)), particularly in the fall phase of the plasma within the jet. These apex substructures were noticeably wider than rest of the jet body, partially due to superimposition of internal shock waves (Mackenzie Dover et al. 2021) and/or accumulation of plasma prior to maximum ascend of the jet. The variations in cross-sectional widths are also suggested in TD plots for zero/weakly tilted jets ($\theta = 0°$, 5°, 10°) in Figure 8. Here, again, the sites for width deformations undergo transitions to transverse pulse-like motions with increasing tilt angles. Concurrent observations of cross-sectional width deformations and transverse motions in chromospheric structures have been reported in previous studies (Jess et al. 2012; Morton et al. 2012; Sharma et al. 2018) as signatures of MHD mode coupling and/or nonlinear kink waves. However, observational verification of the transitions between different kinematic modes and their relationship with the inclination of jet structures, still remains unclear. This is particularly due to the complex chromospheric environment and observational constraints from current instrumentation. Figure 9 highlights the possible observations of internal substructures in a jet for a variety of spatial resolutions. The unresolved sites of plasma coagulation in jets

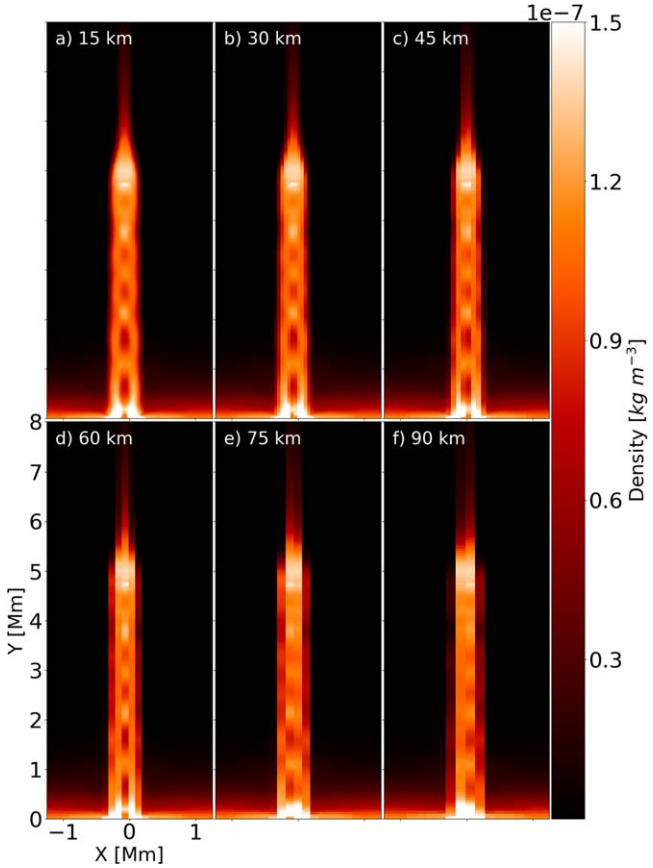

Figure 9. Panels (a)–(f) show the density structure of the simulated jet at different spatial resolution, ranging from 15–90 km. The internal substructures (crisscross/knot-like) tend to become more unresolved with lower spatial sampling, suggesting a possible reason for the lack of observational verification with current instrumentation.

as crisscross patterns from current observations (Figures 9(d)–(f)) could be identified with better resolution (Figures 9(a)–(c)) from upcoming facilities, such as the Daniel K. Inouye Solar Telescope (DKIST; Rimmele et al. 2020; Rast et al. 2021) and European Solar Telescope (EST; Schlichenmaier et al. 2019).

4. Conclusion

This paper investigated the role of misalignment between propagating momentum pulse and ambient magnetic field for a chromospheric type I spicule structure in a stratified lower solar atmosphere. The computational model used here was adapted from Mackenzie Dover et al. (2021), where field-aligned plasma flows in numerical jets were studied. Parameter studies for a combination of misalignment angles (θ), drivers (amplitude, period), and magnetic field (B) magnitudes were analyzed to identify their influence in determining the morphological (height, length, cross-sectional width) and kinematic (longitudinal, transverse) characteristics of type I spicules in a chromospheric environment. The main results of our investigation are:

1. Misalignment between background magnetic field and initial momentum pulse had strong influence on the overall morphology of simulated jets. Maximum apex height and length magnitudes continuously decreased with increasing tilt angles, implying existence of longer jets in regions where mass flows remains strongly aligned

with the magnetic fields. These results were also consistent with the observed cases of chromospheric jet features in coronal holes and quiet-Sun regions.
2. Drop in apex heights and lengths are prominent after $\theta = 20°$, which is the average inclination angle reported for limb spicules. Also, cross-sectional width estimates show an increase in its magnitudes with increasing tilt angles.
3. Our simulations suggested transverse displacements in jet structures for $\theta \geqslant 5°$. These kink motions tend to increase with rise in misalignment angles, while having bright leading edges/nodes. It highlighted higher plasma densities at leading sites as compared to trailing edges.
4. The *standard jet* with field-aligned plasma motions showed complex *crisscross* internal substructures with bright bulb-like apex. These substructures tend to diverge toward the leading edge of jet displacement with increasing misalignment angles, however, retained the bright bulb-like apex structure.
5. The *pulse-like* transverse displacement in simulated jets could be attributed to dynamic kink instability, which is a consequence of dominating centripetal forces over Lorentz force for structures with local curvature and/or misaligned background magnetic field and plasma flows.

This study is a step forward from our previous investigations of numerical jets (spicules) using a simple model of plasma motions along the magnetic fields in a stratified lower solar atmosphere. One of the major outcomes of our analysis is an (alternate) explanation for *pulse-like* transverse motions in chromospheric jets and its coupled evolution with cross-sectional width deformations. These can provide a much sought after insight into the wave mode evolution and/or coupling in jets located in regions with varied background magnetic field topology. We plan, as a next step, to observationally verify the relationship between jet inclinations and the estimated morphological/dynamical characteristics, along with their impact on interpreted wave behavior in lower solar atmosphere. These provide a fruitful avenue for investigation using the highest possible resolution from upcoming facilities (DKIST, EST) in the near future.

F.M. and R.E. acknowledge the support of Science and Technology Facilities Council UK (grant No. ST/M000826/1) and The Royal Society (UK). F.M. is grateful for the STFC studentship. R.S. is grateful for support from the UKRI Future Leader Fellowship (RiPSAWMR/T019891/1). Part of the computations used the Sheffield University HPC cluster ShARC. Numerical results were obtained using the open source software MPI-AMRVAC, mainly developed at K.U. Leuven. Visualizations of the data were done using Python, an open source and community-developed programming language.

ORCID iDs

Fionnlagh Mackenzie Dover https://orcid.org/0000-0002-1984-7303
Rahul Sharma https://orcid.org/0000-0002-0197-9041
Robertus Erdélyi https://orcid.org/0000-0003-3439-4127

References

Anan, T., Kitai, R., Kawate, T., et al. 2010, PASJ, 62, 871
Antolin, P., Schmit, D., Pereira, T. M. D., De Pontieu, B., & De Moortel, I. 2018, ApJ, 856, 44
Asensio Ramos, A., de la Cruz Rodríguez, J., Martínez González, M. J., & Socas-Navarro, H. 2017, A&A, 599, A133
Beckers, J. M. 1968, SoPh, 3, 367
Canfield, R. C., Reardon, K. P., Leka, K. D., et al. 1996, ApJ, 464, 1016
Centeno, R., Trujillo Bueno, J., & Asensio Ramos, A. 2010, in Magnetic Coupling between the Interior and Atmosphere of the Sun, ed. S. S. Hasan & R. J. Rutten (Berlin: Springer), 255
Chen, H.-D., Zhang, J., & Ma, S.-L. 2012, RAA, 12, 573
de la Cruz Rodríguez, J., & Socas-Navarro, H. 2011, A&A, 527, L8
De Pontieu, B., McIntosh, S., Hansteen, V. H., et al. 2007, PASJ, 59, S655
Jess, D. B., Pascoe, D. J., Christian, D. J., et al. 2012, ApJL, 744, L5
Keppens, R., Meliani, Z., van Marle, A. J., et al. 2012, JCoPh, 231, 718
Kriginsky, M., Oliver, R., Freij, N., et al. 2020, A&A, 642, A61
Kuridze, D., Zaqarashvili, T. V., Henriques, V., et al. 2016, ApJ, 830, 133
Leenaarts, J., Carlsson, M., & Rouppe van der Voort, L. 2015, ApJ, 802, 136
Liu, W., Berger, T. E., Title, A. M., & Tarbell, T. D. 2009, ApJL, 707, L37
Mackenzie Dover, F., Sharma, R., & Erdélyi, R. 2021, ApJ, 913, 19
Mackenzie Dover, F., Sharma, R., Korsós, M. B., & Erdélyi, R. 2020, ApJ, 905, 72
Martínez-Sykora, J., De Pontieu, B., Carlsson, M., & Hansteen, V. 2016, ApJL, 831, L1
Martínez-Sykora, J., Hansteen, V., De Pontieu, B., & Carlsson, M. 2009, ApJ, 701, 1569
Morton, R. J., Verth, G., Jess, D. B., et al. 2012, NatCo, 3, 1315
Pereira, T. M. D., De Pontieu, B., & Carlsson, M. 2012, ApJ, 759, 18
Pereira, T. M. D., De Pontieu, B., Carlsson, M., et al. 2014, ApJL, 792, L15
Pereira, T. M. D., Rouppe van der Voort, L., & Carlsson, M. 2016, ApJ, 824, 65
Petralia, A., Reale, F., & Testa, P. 2018, A&A, 609, A18
Porth, O., Xia, C., Hendrix, T., Moschou, S. P., & Keppens, R. 2014, ApJS, 214, 4
Rast, M. P., Bello González, N., Bellot Rubio, L., et al. 2021, SoPh, 296, 70
Rimmele, T. R., Warner, M., Keil, S. L., et al. 2020, SoPh, 295, 172
Schad, T. A., Penn, M. J., & Lin, H. 2013, ApJ, 768, 111
Schlichenmaier, R., Bellot Rubio, L. R., Collados, M., et al. 2019, arXiv:1912.08650
Sharma, R., Verth, G., & Erdélyi, R. 2018, ApJ, 853, 61
Shibata, K., & Uchida, Y. 1985, PASJ, 37, 31
Shibata, K., & Uchida, Y. 1986, SoPh, 103, 299
Skogsrud, H., Rouppe van der Voort, L., De Pontieu, B., & Pereira, T. M. D. 2015, ApJ, 806, 170
Sterling, A. C. 2000, SoPh, 196, 79
Suárez, D. O., Ramos, A. A., & Bueno, J. T. 2015, ApJL, 803, L18
Tóth, G. 1996, ApL&C, 34, 245
Tsiropoula, G., Tziotziou, K., Kontogiannis, I., et al. 2012, SSRv, 169, 181
Verth, G., & Jess, D. B. 2016, Low-Frequency Waves in Space Plasmas, Vol. 216 (New York: Wiley), 431
Xia, C., Teunissen, J., El Mellah, I., Chane, E., & Keppens, R. 2018, ApJS, 234, 30
Zaqarashvili, T. V. 2020, ApJL, 893, L46
Zaqarashvili, T. V., & Erdélyi, R. 2009, SSRv, 149, 355
Zaqarashvili, T. V., Lomineishvili, S., Leitner, P., et al. 2021, A&A, 649, A179